ARTICLE

Possible embryos and precursors of crystalline nuclei of calcium carbonate observed by liquid-cell transmission electron microscopy

Received 00th January 20xx,
Accepted 00th January 20xx

DOI: 10.1039/x0xx00000x

Yuki Kimura,*[a] Hiroyasu Katsuno[b] and Tomoya Yamazaki[c]

Several different building blocks or precursors play important roles in the early stages of the crystallization of calcium carbonate ($CaCO_3$). Many studies have been conducted over a long period to elucidate the fundamental processes involved in this crystallization. Here, we report the role of an amorphous phase and embryo at the beginning of the nucleation of $CaCO_3$ from solutions of relatively low supersaturation. Prenucleation crystals formed in amorphous calcium carbonate (ACC) at a significantly large formation rate of 2×10^{22} m^{-3} s^{-1}, suggesting that a low interfacial energy exists between the ACC and crystals. Only one calcite crystal exceeded the size for a critical nucleus (~10^4 molecules) in 150 pre-nucleation crystals. Each pre-nucleation crystal might consist of a different polymorph, and ACCs have a similar composition and structure. A particle-detection algorithm, used in conjunction with machine learning, suggested that an embryo with a characteristic structure exists in solution and might play a crucial role in nucleation. No similar embryonic structure could be observed immediately after the dissolution of pre-nucleation particles, implying that their dissolution process is not simply the reverse process of their growth. This method should provide a new approach to understanding nucleation processes.

Introduction

By using a liquid cell, solution samples can now be observed by transmission electron microscopy (TEM), permitting the visualization of nanoscale processes in aqueous solutions.[1–3] The technique has allowed us to observe the dynamic processes occurring in the early stages of crystallization that were previously unpredictable and this has stimulated an acceptance of nonclassical concepts in crystallization, including unexpected relationships between precursors and final crystals,[4,5] the relationship between dynamic behaviours of defects and the stability of the resulting crystal,[6] the timing of the dehydration process in crystallization,[7–9] and fluctuation-triggered or fluctuation-selected nucleation.[10,11]

Calcium carbonate ($CaCO_3$) attracts considerable attention because of the complexity of its nucleation due to the appearance of various polymorphs,[12] and because of its use as an industrial material,[13] its action as a reservoir for carbon dioxide,[14] and its role in biomineralization.[15] To discuss the early stages of crystallization, we use the calcium carbonate as a model substance in view of the variety of polymorphs present in its nucleation process. In the case of nucleation of calcium carbonate from aqueous solutions of relatively high supersaturation, the formation of an amorphous phase before that of a crystalline phase has long been known.[16] Solution-mediated phase transition from an amorphous phase into a crystalline phase has been directly observed by optical microscopy.[17] In general, it is believed that Ostwald's rule of stages holds in many cases. A contribution of pre-nucleation clusters to the nucleation has also been reported.[18] An identification of the existence of pre-nucleation clusters by using cryo-TEM has been claimed,[19] but this claim is controversial.[20]

Here, we have attempted to understand the roles of the amorphous phase and an embryo phase in the early stages of crystallization by two different approaches. The first was the observation of amorphous calcium carbonate (ACC) produced by mixing two solutions in a liquid cell TEM (LC-TEM), because ACC is a typical precursor of crystalline phases.[15,21] The second was the detection of an embryo during dissolution and precipitation of calcium carbonate by means of a machine-learning particle-detection algorithm.

Formation of ACC by mixing of two solutions. Although LC-TEM is a powerful tool for observing crystallization processes in aqueous solution, the experimental conditions are determined by the specific constraints of TEM, such as the thickness of the solution as controlled by spacers (typically 50–500 nm), the volume of the solution (0.1–1 nL), radiolysis by the electron beam,[22,23] the time required from preparation to observation (several minutes), and the temporal resolution of the recorded images (generally less than the video-frame rate).

[a] *Institute of Low Temperature Science, Hokkaido University, Kita-19, Nishi-8, Kita-ku, Sapporo, 060-0819, Japan.*

Electronic Supplementary Information (ESI) available: [details of any supplementary information available should be included here]. See DOI: 10.1039/x0xx00000x

Capturing the early stages of crystallization often requires a great deal of ingenuity. Mixing two different liquids can create a large driving force towards crystallization at certain times. Nevertheless, the direct observation of the moment of nucleation is still difficult, because the mixing initially takes place outside the area of the observation window, so that nucleation occurs before the mixed solution flows into the observable area. We therefore observed the produced ACC particles, which are believed to act as precursors of crystalline calcium carbonate, by LC-TEM.

Detection of embryos by machine learning. One aim of observing a dissolution process is to identify differences between nucleation and dissolution processes. We show, here, competing processes in the formation and dissolution of pre-nucleation particles/crystals of calcium carbonate with diameters of less than 10 nm. These processes were captured in high-resolution TEM (HRTEM) images. To understand the behaviours of embryos and pre-nucleation particles/crystals, we used a machine-learning particle-detection algorithm in conjunction with time-resolved sequential HRTEM images. We define an embryo as a possible cluster of calcium carbonate molecules that has no clear interfaces with the solution and is therefore difficult to recognize as a particle in an HRTEM image. If the nucleus maintains its composition and structure in both growth and dissolution, growing embryos should be detectable by using a particle-detection algorithm, trained with ghost images recorded after dissolution of pre-nucleated particles/crystals as a training dataset.

Experimental procedure

TEM observations. A 3 mM aqueous solution of calcium chloride ($CaCl_2$) and a 3 mM aqueous solution of sodium carbonate (Na_2CO_3) were both flowed into a liquid cell in a Poseidon holder (Protochips, Morrisville, NC) at a rate of 2 μL min^{-1} so that the liquids mixed while under TEM observation at room temperature (23°C). To permit liquid flow, the thickness of the solution in the liquid cell was controlled by means of four spacers, each with a thickness of 150 or 500 nm, situated at the corners of the liquid cell; the actual thickness of the liquid layer was somewhat larger due to bulging of the cell walls caused by the vacuum present in TEM.[24] The TEMs used in this study were a Hitachi H-8100 (200 kV, tungsten filament) with an XR-611B TEM camera (Advanced Microscopy Techniques Corp., Woburn, MA) connected to a conventional digital video recorder, and a Hitachi HF-3300 (300 kV, field-emission gun) with an ORIUS SC1000 CCD TEM camera (Gatan Inc., Pleasanton, CA). The in-situ TEM images were recorded at ~8 and 10 frames per second (fps), respectively.

Machine learning. We have previously developed a low-dose-electron observation method that uses machine learning to reduce the effect of radiolysis by the electron beam,[25] together with a method for the early detection of nucleation events by machine learning that permits efficient observations on small solution volumes (or small observation areas).[26] On the basis of these previous studies, we have now developed a machine-learning program that uses a standard *YOLOv5* algorithm (https://github.com/ultralytics/yolov5) to detect particles in a dataset of in situ TEM images. Annotation was performed by using the open-source program, *LabelImg* (https://github.com/tzutalin/labelImg) For training and validation, we used different 40 s portions of a single 10 fps

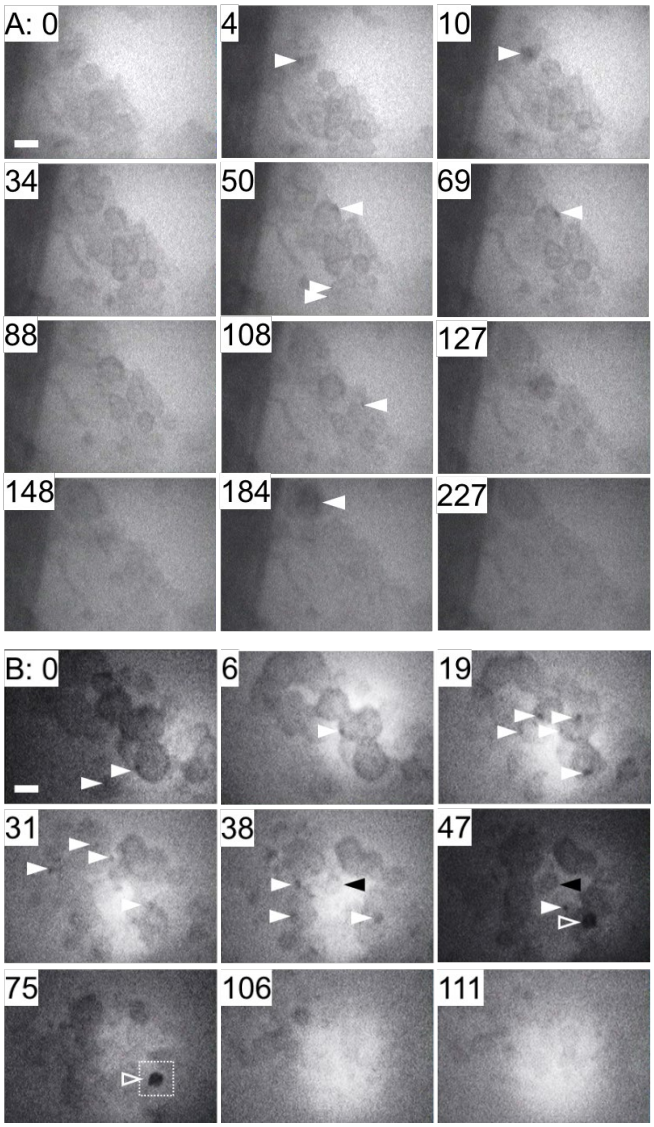

Fig. 1 Time-resolved bright-field TEM (Hitachi H-8100 TEM) images showing the formation of $CaCO_3$ crystals in ACCs. The spacer thickness of the liquid cell was 150 nm. The numbers are the observation times in seconds after the first image, which was recorded immediately after starting electron-beam irradiation. **A**. Constant electron dose rate during the observation. **B**. Variable electron dose rate during the observation. The white arrowheads indicate regions of stronger contrast than that of the initial particle, suggesting the formation of denser particles, i.e., crystals. The black arrowheads in **B** indicate the formation of an amorphous particle. The open arrowheads indicate a crystal with longer lifetime. The dotted square region has been magnified in **Fig. 2.** Scale bars: 50 nm.

video recording. The *YOLO* algorithm for object detection works effectively with TEM images.[26] We prepared training datasets for the detection of pre-nucleation particles or embryos. The images were extracted from HRTEM observations captured as video recordings.

First, individual particles that had clear interfaces with the solution were annotated to confirm that the algorithm was capable of detecting particles. Secondly, we identified images that showed the formation of a pre-nucleation particle, and we annotated the same position in the images recorded 0.1, 0.3, 0.5, 0.7, and 1 s before the formation of the particle. If the embryo of calcium carbonate has a characteristic structure before nucleation, we should have been able to detect this embryo before a nucleation event occurred. Thirdly, we identified images in which a pre-nucleation particle dissolved, and we annotated the same position in the images recorded at 0.1, 0.5, 1, and 1.5 s after the disappearance of the pre-nucleation particle by dissolution. If the dissolution process of calcium carbonate is the same as the formation process, the embryo for the formation process should be capable of being detected after the disappearance of the pre-nucleation particle.

Results and discussion

Formation of ACC. Approximately 15 min after starting the liquid flow, particles with a rounded shape and size of less than 100 nm in diameter were observed by TEM (0 s in **Fig. 1A** and **Video 1**). Those particles did not fuse to each other like liquid droplets, suggesting the presence of a solid phase. In addition, because those solid particles exhibited no diffraction contrast, they were amorphous in nature. Of the two possible precursor forms, ACC[15,21] or dense liquid,[27,28] these features suggest that the particles consist of ACC with a spherical shape rather than a dense liquid.

The ACC particles gradually expanded and their contrast became relatively weaker at the interior and stronger at the periphery. Then, intense contrasts appeared from the inside the ACC, as shown by the white arrowhead at 4 s in **Fig. 1A** or, more clearly, in **Video 1**. The contrast of the particle became stronger at 10 s. This intense contrast corresponds to a diffraction contrast originating from a crystal. Soon after, the intense contrast disappeared. A similar phenomenon involving the appearance and disappearance of crystals has been observed for ACC. All ACC particles disappeared after four minutes (**Fig. 1A** and **Video 1**). The electron dose rate had a constant value of approximately 4×10^3 electrons nm^{-2} s^{-1} and, therefore, the total dose was ~1×10^6 electrons nm^{-2}. Electron irradiation at a dose rate of 4×10^4 electrons $nm^{-2}s^{-1}$ for 300 s has been shown to cause decomposition of $CaCO_3$ to CaO and CO_2[29] whereas a dose rate of 6×10^3 electrons nm^{-2} s^{-1} does not do so.[30] Our electron dose rate was below the second lower value.

All crystals were formed from the interior and/or inner surface of ACC. We did not observe direct nucleation of crystalline particles from the solution under our experimental conditions (**Videos 1 and 2**). Instead, an amorphous particle formed from the solution in the central part of the aggregate in the second observation, as shown by the black arrowheads in **Fig. 1B**. This might be because the dissolution of ACCs results in a transient flow of the solution towards the area indicated by the black arrowheads in **Fig. 1B**. The inertia of the flow increases the concentration sufficiently to exceed the critical concentration required for nucleation of ACC. This suggests that there is a local inhomogeneity in concentration in the region of the solution where a cluster of ACC exists. In other words, the distribution of ACC in the solution enhanced any inhomogeneities in the concentration of the solution. Finally, all particles disappeared.

Effects of electron irradiation. In the second series of observations, shown in **Fig. 1B**, the electron dose rate was reduced from 7×10^3 electrons nm^{-2} s^{-1} at 2–40 s to 1×10^3 electrons nm^{-2} s^{-1} at 41–105 s to suppress the effects of electron irradiation. After 106 s, the electron dose rate was increased to 6×10^3 electrons nm^{-2} s^{-1} to confirm the dissolution of ACC from brighter images. Under the higher (7×10^3 electrons nm^{-2} s^{-1}) and lower (1×10^3 electrons nm^{-2} s^{-1}) electron dose rates, the maximum radius (8.8 ± 1.9 nm and 9.0 ± 4.0 nm, respectively), the growth rate (20.6 ± 10.8 nm s^{-1} and 15.7 ± 9.0 nm s^{-1}, respectively), and the dissolution rate (7.4 ± 3.1 nm s^{-1} and 9.5 ± 5.6 nm s^{-1}, respectively) in averaged values of the crystals were similar within a standard deviation (one sigma). All these three values should be dependent on the saturation level. The similarity of these values therefore suggests that the effects of electron irradiation on the solution are not different at all the dose rates that we used.

Formation of pre-nucleation crystals and calcite nuclei. In **Fig. 1B,** the lifetimes of the formed crystals at higher and lower electron dose rates do also not differ, (1.6 ± 1.3 and 2.0 ± 1.4 s, respectively), apart from one long-lived particle with a lifetime of 49.4 s, as shown by the open white arrowheads in **Fig. 1B**. The face angle of the largest crystal was 75°, which corresponds to the characteristic face angle of calcite, as shown in the

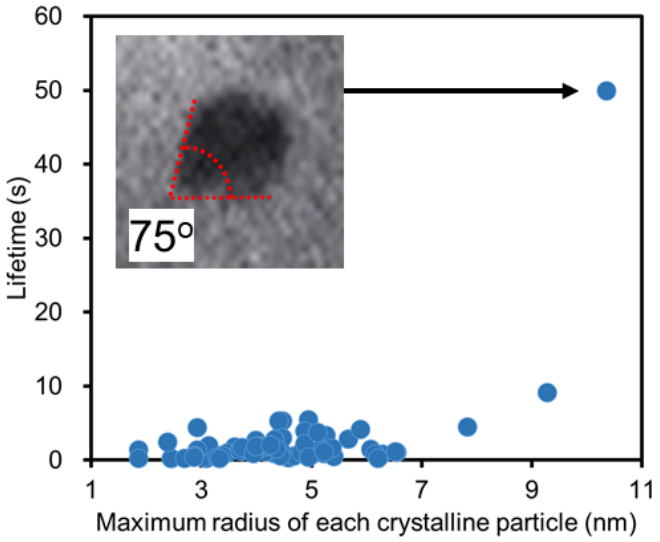

Fig. 2. Size dependence of the crystalline lifetime. The insert is an enlarged image of the largest crystal, indicated by the open white arrowheads, in **Fig. 1B**. This larger crystal has a face angle of 75°, corresponding to the typical face angle of calcite.

enlarged image in **Fig. 2**. The formation of calcite from the interior of ACC was not observed in a previous LC-TEM study.[12] This large crystal dissolved after the dissolution of the surrounding ACC. These results suggest that only this single calcite crystal exceeded the size of a critical nucleus, whereas others dissolved because the surface-free-energy disadvantage was greater than the bulk-free-energy advantage. All the smaller crystals were therefore pre-nucleation crystals.

The size dependence of the lifetime of the produced crystals shows that all pre-nucleation crystals smaller than 8 nm in radius had a lifetime of less than 5.5 s (**Fig. 2**). The average lifetime and its deviation have almost constant values, suggesting that they are independent of the size. If the pre-nucleation crystal consisted entirely of calcite, its lifetime should have increased with increasing size. However, the results did not show such a trend. This can be explained by considering the formation of various polymorphs of pre-nucleation crystals with different bulk solubilities. Namely, pre-nucleation crystals probably do not only calcite, but other polymorphs, such as aragonite and vaterite, are present. These might form at differing rates in ACC. Another possibility is that the structure of the smaller crystals is still under construction and, therefore, contains many defects, resulting in differences in the stabilities of the smaller crystals. It may be able to rephrase that the relaxation time of the structure takes longer relative to the growth rate, as expected to be like the glass transition.

The size of the critical nucleus of calcite in ACC is around 9–10 nm under our experimental conditions. Calcite nuclei of critical size therefore contain approximately 5×10^4 molecules of $CaCO_3$. To achieve or detect nucleation within a realistic timescale in a laboratory, experiments have generally been conducted under conditions of high supersaturation. The size of critical nuclei under such supersaturation conditions is less than 10^3 molecules.[31] The size of the critical nucleus of 5×10^4 $CaCO_3$ molecules in the current experiment was significantly larger than that under typical experimental conditions. The larger size of the critical nucleus suggests that the supersaturation of calcite to ACC is smaller than that to solution. Calcite does not form from the solution despite being supersaturated, probably because of the high interfacial energy.

The role of ACC as a precursor. We observed the formation of pre-nucleation crystals in the ACC at a rate of 1.3 s^{-1} (**Fig. 1**). If the particle shape is assumed to be spherical, the formation rate of pre-nucleation crystals was 2×10^{22} m^{-3} s^{-1} in the ACC. This apparently large value can be explained by the small interfacial energy between calcite (or other polymorphs) and ACC. Comparing ACC and solution, the structure of ACC is closer to the structure of calcite than to that of the solution. Therefore, the interfacial energy between calcite and ACC should be smaller than that between calcite and the solution. However, only one crystal of a size that exceeded that of a critical nucleus was observed among 150 pre-nucleation crystals. Consequently, the nucleation rate of calcite in the ACC is approximately 10^{20} m^{-3} s^{-1}.

It is surprising that a crystal consisting of as many as 10^3 molecules can form within a few seconds in an amorphous particle at a significantly large rate of 10^{22} m^{-3} s^{-1}. This might be explained by the diffusion coefficient of calcium and carbonate ions in ACC being so large that the ACC behaves in a fluid manner. However, the existence of high fluidity is contrary to the observed fact that ACC particles do not fuse to each other. Another possibility is that there are many water-filled voids in the ACC that facilitate the transport of molecules and induce a large inhomogeneity of concentration. Indeed, it has been reported that voids present in ACC contain mobile water.[30]

It has been proposed that ACCs have polymorphs with a structural similarity to such crystalline phases as calcite and vaterite.[32] Since the clusters of ACCs in **Fig. 1** exist in the same place, their solubilities should be similar. Therefore, their composition and local structure should also be similar. Nevertheless, the results regarding the formation of various polymorphs imply that there is less correlation between the structure of the ACC and the polymorphism of $CaCO_3$.

Phenomena that possibly differ from the classical view. When the size of the crystal is smaller than a critical size, its growth rate should be smaller than the absolute value of its dissolution rate. This is because growth is a stochastic process based on thermal fluctuations, whereas dissolution is close to being deterministic. In our observation, the result was the opposite: the growth rate was larger than the absolute value of the dissolution rate. At the time of the formation of a crystal, the concentration should be relatively high and, therefore, the thermodynamic energy barrier could be more easily overcome. Once a crystal forms, the concentration surrounding the crystal becomes lower than the equilibrium concentration of the crystalline phase, and then, the crystal starts to dissolve more slowly than it grows, because the surrounding ACC also dissolves.

Observation of pre-nucleation processes in HRTEM images. **Fig. 3** shows an aragonite crystal, which is one of the

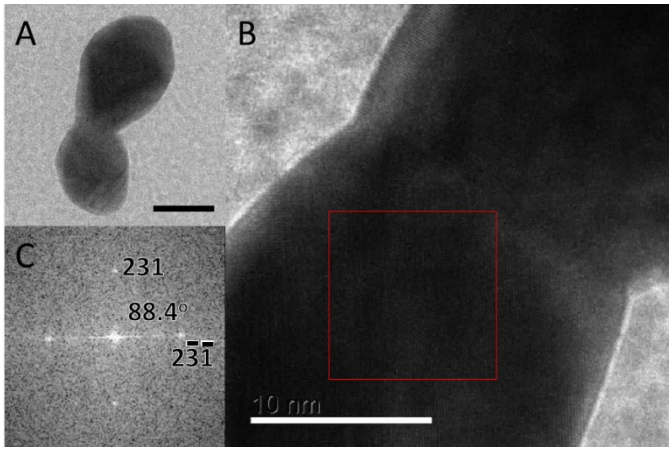

Fig. 3. Mother crystal for the dissolution and precipitation experiment. A. Micrograph of the complete mother crystal. The scale bar is 20 nm. B. Lattice image of the mother crystal. The scale bar is 10 nm. C. Fast-Fourier-transform image corresponding to the red square in B. The spots correspond to the {231} planes of aragonite (JCPDS card # 41-1475) crossing at an angle of 88.4°.

polymorphs of $CaCO_3$, used in dissolution and precipitation experiments in a liquid cell with a spacer of 500 nm, subjected to HRTEM observations by an HF-3300 TEM with a field-emission gun, operated at an acceleration voltage of 300 kV. The solution did not flow, i.e., the solution concentration was maintained by the solubility of the aragonite crystal.

When the magnification was increased from that shown in **Fig. 3a** to that shown in **Fig. 4**, the aragonite began to dissolve because the pH of the solution decreased as a result of the intense electron dose.[22] Because the solubility of $CaCO_3$ increases with decreasing pH,[33] aragonite dissolved until the solution condition reached equilibrium. Then, two different kinds of object precipitated near the crystal (**Fig. 4** and **Video 3**). One was a thin crystal that nucleated heterogeneously on the amorphous silicon nitride window of the liquid cell (**Figs. 4A–C**). The other was a particle that nucleated homogeneously around the crystal (**Fig. 4D**). Both these rapidly disappeared, like the pre-nucleation crystals formed from ACC shown in **Fig. 1**, suggesting that these tiny particles were also prenucleation crystals/particles.

Thin crystals formed throughout the view at a formation rate of 1.9×10^{15} m^{-2} s^{-1} and with a lifetime of less than 0.3 s. Assuming they were spherical, their average radius was 6.2 nm. They had various lattice constants and the polymorphs present were not identified with ikaite, CaO, and $Ca(OH)_2$. The thin crystal shown in **Figs. 4A–C** with lattice fringes of ~0.5 nm might consist of calcite viewed from the *a*-axis.

The formation rate of the three-dimensional particles, as shown in Fig. 4D, was 1.9×10^{15} m^{-2} s^{-1} and, assuming they were spherical, their average radius was 2.7 nm. Some of the pre-nucleated particles had diffraction contrasts originating from crystals. Their lifetime was less than 2 s and was typically 0.3 s, suggesting these particles were also smaller than the size of a critical nucleus. The lifetime of these particles showed no size dependency, like the crystals formed from ACC shown in **Figs. 1** and **2**. The crystalline structure and/or crystallinity of the pre-nucleated particles might vary regardless of the system. Particles formed slightly further from the crystal, even though the concentration was expected to decrease in this region. We hypothesize that a hydrated layer is present on the crystal and might prevent the precipitation of particles in this region. The biggest difference from the case shown in **Fig. 1** is that the crystals appeared from the solution directly and did not appear via ACC.

Detection of pre-nucleation particles by machine learning. To confirm the applicability of our particle-detection algorithm for HRTEM images, particles were detected after training with annotated data. Examples of annotated particles are shown in **Fig. 5A**, and results of the validation are shown in **Fig. 6**. The precision score and the recall score reached 0.82 and 0.73, respectively.

Detection of embryos by machine learning. To detect embryo and to predict nucleation events from a solution, potential embryos were annotated as shown in **Fig. 5B** for machine learning. An embryo is defined as a cluster, possibly consisting of $CaCO_3$, that has no clear interfaces with the solution, as shown by the blue and yellow squares in **Fig. 5**. Therefore, it is difficult to recognize as a particle in an HRTEM image. Pre-nucleation particles, on the other hand, have clear interfaces, as shown by the red squares in **Fig. 5**. Examples of results of

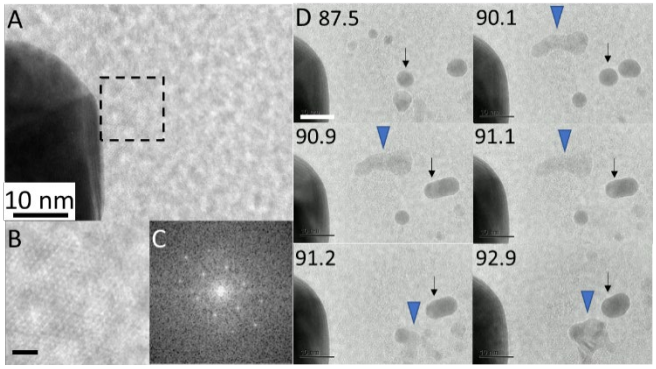

Fig. 4. Two different kinds of pre-nucleation crystals. A. Thin crystal two-dimensionally precipitated on the window of amorphous silicon nitride. B. Magnified image corresponding to the dashed square region. The scale bar is 2 nm. C. Fast-Fourier-transform images corresponding to the magnified image. D. Pre-nucleation crystals three-dimensionally precipitated in the solution. The numbers indicate the time after the observation area and magnification were fixed. The arrows show a particle that merged on contact with another particle. The blue arrowheads show an object that heterogeneously coagulated on the three tiny particles seen at 87.5 s and, then, dissolved at 91.1–91.2 s. Simultaneously, another object with a similar contrast heterogeneously coagulated on the bottom particle at 91.2 s. This appears to correspond to dissolution and precipitation of the object. The scale bar is 10 nm for D.

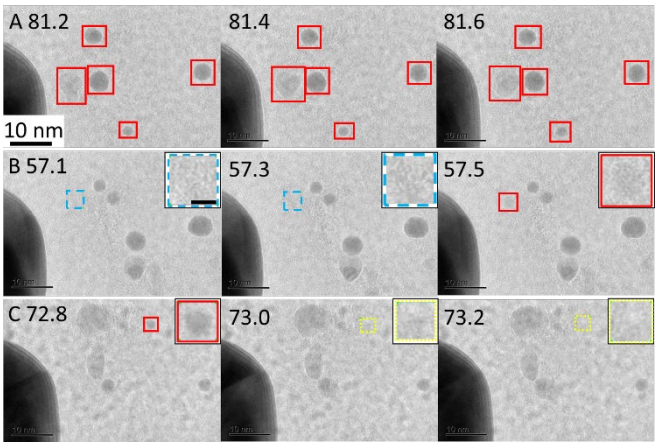

Fig. 5. Examples of annotation in HRTEM images. The numbers indicate the time after the observation area and magnification were fixed. A. Annotation for particle detection. B. An embryo has been annotated, as indicated by the blue dashed square, to detect embryos. The red square at the last panel at 57.5 s corresponds to a particle. The inserts are enlarged images of the squares in each panel. The scale bar in the enlarged image at 57.1 s is 2 nm, and is same for all the enlarged images. C. A ghost has been annotated, as indicated by the yellow dotted square, to detect embryos.

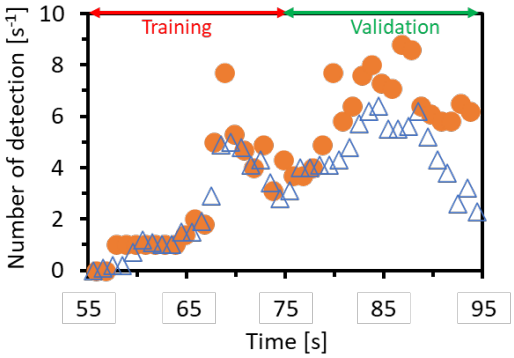

Fig. 6. Number of particles detected per second in **Video 3.** The circles and triangles represent labels applied manually and those detected by machine learning, respectively. The datasets at 55–75 s and 75–93 s were used for training and validation, respectively.

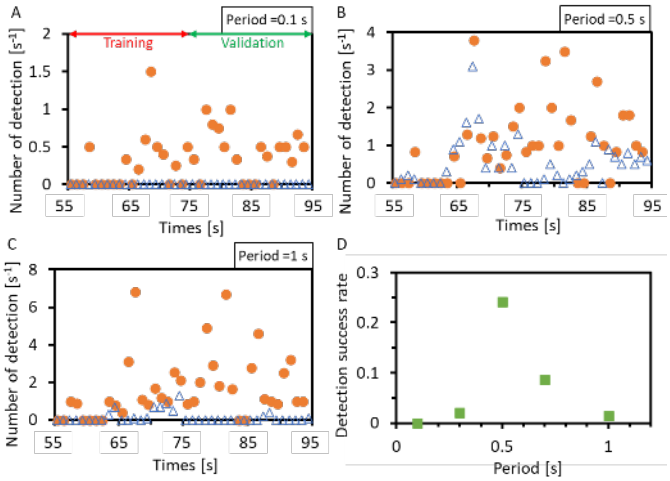

Fig. 7. Number of embryos detected per second in **Video 3**. The circles and triangles represent labels applied manually and detected by the machine learning, respectively. The datasets at 55–75 s and 75–93 s were used for training and validation, respectively. A–C. Examples of detections for periods of 0.1, 0.5, and 1 s, respectively. D. The ratio of the number of detections to the number of labels in the validation.

training and validation for the periods 0.1, 0.5, and 1 s are shown in **Figs. 7A**–**C**, respectively. The filled circles and open triangles represent labels applied manually and those detected by machine learning, respectively. Almost no items were detected in **Figs. 7A** and **7C**. In **Fig. 7B**, machine-learning reproduces the labelled data in the training, and detected several objects during the validation. For a quantitative comparison, we plotted the number of detections over the number of labels (**Fig. 7D**). The abscissa represents the annotation period just before the nucleation event. The number of detections in the period 0.5 s is obviously larger than that in other periods. After detection using the model parameter for the period 0.5 s, nucleation sometimes occurred, as shown in **Fig. 5B**.

In ordinary machine learning, the larger the number of datasets, the better the accuracy of the machine learning. In the

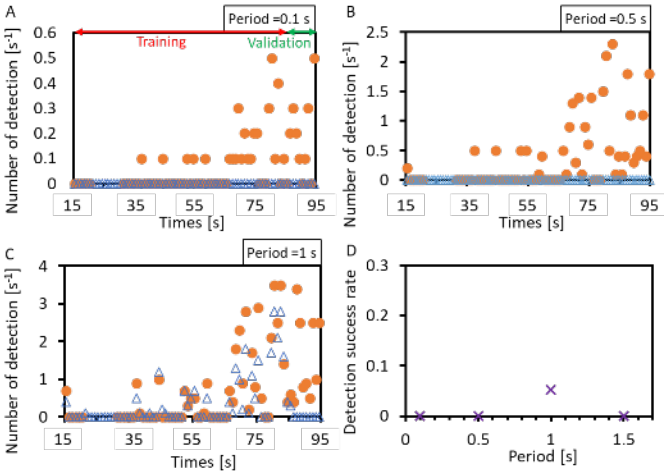

Fig. 8. Number of embryos detected per second in **Video 3**. The circles and triangles represent labels applied manually and detected by machine learning, respectively. The datasets at 0–85 s and 85–93 s were used for training and validation, respectively. A–C. Examples of detections for periods of 0.1s, 0.5, and 1 s, respectively. D. The ratio of the number of detections to the number of labels in the validation.

case of the 0.1 s period, no embryos were detected, possibly because the number of training datasets was insufficient to permit their detection (**Fig. 7A**). In the case of the 0.5 s period, 25% of embryos were detected by machine learning (**Fig. 7B**), suggesting that embryos with a characteristic structure related to that of the pre-nucleation crystals were present in the solution. In the case of the 0.7 s period, the ratio of the number of detections to the number of labels in the validation decreased to 10%. Finally, in the case of the 1 s period, no embryos were detected, despite a larger number of datasets. These results suggest that the dataset is incorrect when the period becomes too long. Consequently, the embryo must form ~0.5 s before the formation of the pre-nucleation crystal in this system.

Detection of embryos using an algorithm for detection of ghosts. By using a similar method to the above, we also attempted to detect embryos by using the algorithm to detect ghosts present after the disappearance of particles. However, no embryos were detected in training or validation in any of the training periods of 0.1, 0.5, 1, and 1.5 s after the dissolution of pre-nucleation crystals, as shown in **Fig. 8**. There are two possible explanations for this. The first is that the dissolution process involves different structural changes to the growth process, i.e., dissolution is not the reverse process of growth. The other reason is a difference in the timescale, i.e., the dissolution process might be terminated within 0.1 s. This is consistent with our observation that particles with sizes of the order of several nanometres disappear within 0.1 s. The dissolution of the particles is complete in a shorter timescale than that required for their growth. In addition, the fact that the algorithm cannot detect even ghosts suggests that no characteristic structure exists in the timescale longer than 0.1 s

after dissolution. It is probably impossible to detect them at the current temporal resolution of our system.

Conclusions

Pre-nucleation processes in crystallization of calcium carbonate $CaCO_3$ were directly visualized under near-equilibrium conditions by LC-TEM. Several different building blocks or precursors, such as amorphous, pre-nucleation particles/crystals, and embryos, play roles near the beginning of nucleation of $CaCO_3$. Pre-nucleation crystals formed in ACC with a significantly large formation rate of 2×10^{22} m^{-3} s^{-1}, suggesting a lower interfacial energy between ACC and crystals. Among 150 prenucleation crystals, only one calcite crystal exceeded the size for a critical nucleus (~10^4 molecules). The lifetime of the pre-nucleation crystals was independent of their size, implying that several different polymorphs formed in the ACC as pre-nucleation crystals. Since the ACC particles existed in the same area, their solubilities should be identical, and therefore their compositions and local structures should all be identical. These results imply that ACC has no polymorphs related to the various crystalline polymorphs, such as calcite or vaterite.

When a particle-detection algorithm based on machine learning was applied to a video captured by HRTEM observations, the results suggest the existence of embryos with a characteristic structure and the lifetime of ~0.5 s in a solution that might play a crucial role in nucleation. No related embryonic structure remained immediately after the dissolution of a pre-nucleation particle/crystal, suggesting that the dissolution process does not follow the same structural path as the growth process, or that the timescale for the dissolution process is much shorter than that of the growth process.

Author Contributions

Y.K. conceivedthe presented idea. Y.K. and T.Y. performed the TEM observations. H.K. designed the computational framework. Y.K. analysed the data and wrote the manuscript. All the authors contributed to the final manuscript.

Captions for supplementary videos

Video 1. In-situ TEM observation of the formation of calcium carbonate crystals in ACCs. This video is 10× actual speed. The scale bar is 40 nm. Frames of the same event are presented in **Fig. 1A**.

Video 2. In-situ TEM observation of the formation of calcium carbonate crystals in ACCs. This video is 10× actual speed. The scale bar is 50 nm. Frames of the same event are presented in **Fig. 1B**.

Video 3. In-situ HRTEM observation of the precipitation of two different kinds of pre-nucleation crystals. This video is 4× actual speed. Frames of the same event are presented in **Fig. 4**.

Conflicts of interest

The authors declare no competing interests.

Acknowledgements

This work was partly supported by Grants-in-Aid for Scientific Research (S) from KAKENHI (15H05731 and 20H05657). The authors thank to M. Shizuka Hirakawa of the Institute of Low Temperature Science, Hokkaido University, for supporting the production of annotation data for the machine learning, and Manabu Shirai and Hiroaki Matsumoto of Hitachi High-Tech Co. for HRTEM observations.

References

1 N. de Jonge and F. M. Ross, *Nat. Nanotechnol.*, 2011, **6**, 695.
2 J. M. Yuk, J. Park, P. Ercius, K. Kim, D. J. Hellebusch, M. F. Crommie, J. Y. Lee, A. Zettl and A. P. Alivisatos, *Science*, 2012, **336**, 61.
3 H.-G. Liao, L. Cui, S. Whitelam and H. Zheng, *Science*, 2012, **336**, 1011.
4 D. Li, M. H. Nielsen, J. R. I. Lee, C. Frandsen, J. F. Banfield and J. J. De Yoreo, *Science*, 2012, **336**, 1014.
5 L. Houben, H. Weissman, S. G. Wolf and B. Rybtchinski, *Nature*, 2020, **579**, 540
6 T. Yamazaki, A. E. S. Van Driessche and Y. Kimura, *Soft Matter*, 2020, **16**, 1955.
7 T. Yamazaki, Y. Kimura, P. G. Vekilov, E. Furukawa, M. Shirai, H. Matsumoto, A. E. S. Van Driessche and K. Tsukamoto, *Proc. Natl. Acad. Sci. U. S. A.*, 2017, **114**, 2154.
8 F. Sebastiani, S. L. P. Wolf, B. Born, T. Q. Luong, H. Cölfen, D. Gebauer, M. Havenith, *Angew. Chem. Int. Ed.*, 2017, **56**, 490.
9 J. T. Avaro, S. L. P. Wold, K. Hauser and D. Gebauer, *Angew. Chem. Int. Ed.*, 2020, **59**, 6155.
10 K. Nakajima, T. Yamazaki, Y. Kimura, M. So, Y. Goto and H. Ogi, *J. Phys. Chem. Lett.*, 2020, **11**, 6176.
11 Y. Kimura, H. Niinomi, K. Tsukamoto and J. M. García-Ruiz, *J. Am. Chem. Soc.*, 2014, **136**, 1762.
12 M. H. Nielsen, S. Aloni and J. J. De Yoreo, *Science*, 2014, **345**, 1158.
13 J. Rieger, M. Kellermeier and L. Nicoleau, *Angew. Chem. Int. Ed.*, 2014, **53**, 12380.
14 J. A. Kleypas, R. W. Buddemeier, D. Archer, J.-P. Gattuso, C. Langdon and B. N. Opdyke, *Science*, 1999, **284**, 118.
15 L. Addadi, S. Raz and S. Weiner, *Adv. Mater.*, 2003, **15**, 959.
16 T. Ogino, T. Suzuki and K. Sawada, *Geochim. Cosmochim. Acta*, 1987, **51**, 2757.
17 J. Kawano, N. Shimobayashi, M. Kitamura, K. Shinoda and N. Aikawa, *J. Cryst. Growth*, 2002, **237–239**, 419.
18 D. Gebauer and H. Cölfen, *Nano Today*, 2011, **6**, 564.
19 E. M. Pouget, P. H. Bomans, J. A. C. M. Goos, P. M. Frederik, G. de With and N. A. Sommerdijk, *Science*, 2009, **323**, 1455.
20 P. J. M. Smeets, A. R. Finney, W. J. E. M. Habraken, F. Nudelman, H. Friedrich, J. Laven J. J. De Yoreo, P. M. Rodger and N. A. J. M. Sommerdijk, *Proc. Natl. Acad. Sci. U. S. A.*, 2017, **114**, E7882.
21 M. P. Schmidt, A. J. Ilott, B. L. Phillips and R. J. Reeder, *Cryst. Growth Des.*, 2014, **14**, 938.
22 N. M. Schneider, M. M. Norton, B. J. Mendel, J. M. Grogan, F. M. Ross and H. H. Bau, *J. Phys. Chem. C*, 2014, **118**, 22373.
23 B. Ambrožič, A. Prašnikar, N. Hodnik, N. Kostevšek, B. Likozar, K. Ž. Rožman and S. Šturm, *Chem. Sci.*, 2019, **10**, 8735.
24 M. E. Holtz, Y. C. Yu, J. Gao, H. D. Abruna and D. A. Muller, *Microsc. Microanal.*, 2013, **19**, 1027.
25 H. Katsuno, Y. Kimura, T. Yamazaki and I. Takigawa, *Microsc. Microanal.*; DOI: 10.1017/S1431927621013799.
26 H. Katsuno, Y. Kimura, T. Yamazaki and I. Takigawa, *Front. Chem.*, 2022, **10**, 818230.

27 A. F. Wallace, L. O. Hedges, A. Fernandez-Martinez, P. Raiteri, J. D. Gale, G. A. Waychunas, S. Whitelam, J. F. Banfield and J. J. De Yoreo, *Science*, 2013, **341**, 885.
28 J. T. Avaro, S. L. P. Wolf, K. Hauser and D. Gebauer, *Angew. Chem. Int. Ed.*, 2020, **59**, 6156.
29 C. Rodriguez-Navarro, E. Ruiz-Agudo, A. Luwue, A. B. Rodriguez-Navarro and M. Ortega-Huertas, *Am. Mineral.* 2009, **94**, 578.
30 H. Du, M. Steinacher, C. Borca, T. Huthwelker, A. Murello, F. Stellacci and E. Amstad, *J. Am. Chem. Soc.*, 2018, **140**, 14289.
31 Q. Hu, M. H. Nielsen, C. L. Freeman, L. M. Hamm, J. Tao, J. R. I. Lee, T. Y. J. Han, U. Becker, J. H. Harding, P. M. Dove and J. J. De Yoreo, *Faraday Discuss.*, 2012, **159**, 509.
32 J. H. E. Cartwright, A. G. Checa, J. D. Gale, D. Gebauer and C. I. Sainz-Diaz, *Angew. Chem. Int. Ed.*, 2012, **26**, 11960.
33 P. W. Hart, G. W. Colson, J. Burris, *J. Sci. Technol. For. Prod. Processes*, 2011, **1**, 67.

